ACS OMEGA

http://pubs.acs.org/journal/acsodf

Article

Experimental Study of the Influence of CH_4 and H_2 on the Conformation, Chemical Composition, and Luminescence of Silicon Quantum Dots Inlaid in Silicon Carbide Thin Films Grown by Remote Plasma-Enhanced Chemical Vapor Deposition

Rodrigo León-Guillén, Ana Luz Muñoz-Rosas, Jesús A. Arenas-Alatorre, Juan Carlos Alonso-Huitrón, Ana Laura Pérez-Martínez, and Arturo Rodríguez-Gómez*

Cite This: *ACS Omega* 2022, 7, 19640−19647

Read Online

ACCESS | Metrics & More | Article Recommendations | Supporting Information

ABSTRACT: Silicon carbide (SiC) has become an extraordinary photonic material. Achieving reproducible self-formation of silicon quantum dots (SiQDs) within SiC matrices could be beneficial for producing electroluminescent devices operating at high power, high temperatures, or high voltages. In this work, we use a remote plasma-enhanced chemical vapor deposition system to grow SiC thin films. We identified that a particular combination of 20 sccm of CH_4 and a range of 58−100 sccm of H_2 mass flow with 600 °C annealing allows the abundant and reproducible self-formation of SiQDs within the SiC films. These SiQDs dramatically increase the photoluminescence-integrated intensity of our SiC films. The photoluminescence of our SiQDs shows a normal distribution with positive skewness and well-defined intensity maxima in blue regions of the electromagnetic spectrum (439−465 nm) and is clearly perceptible to the naked eye.

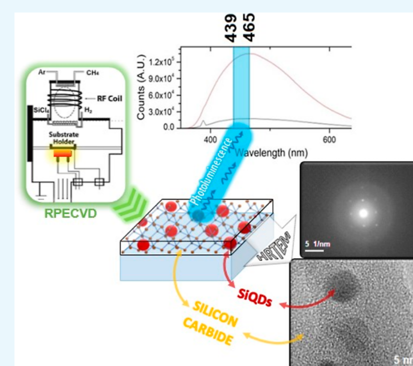

1. INTRODUCTION

Silicon is the second most abundant element in the earth's crust and the backbone of the microelectronics industry.[1,2] When silicon is reduced to sizes smaller than its exciton Bohr radius (<4.5 nm), it exhibits intense and tunable photoluminescence (PL). Experimental and theoretical studies have shown that quantum confinement effects (QCEs) are largely responsible for the observed PL.[3−9] Luminescence from the nanostructured silicon has a vast number of applications. Therefore, systems conformed by silicon quantum dots (SiQDs) embedded in silicon-based matrixes have been of great interest for the scientific and technological community in recent years.[10−19]

On the other hand, silicon carbide (SiC), best known for its use in abrasives[20] and as a reinforcing material,[21] has now become an extraordinary photonic material.[22] One of the most promising applications of SiC is the color centers generated by defects in the crystal, which are excellent candidates for memory and quantum communication applications.[23−25] Additionally, SiC has more than 250 crystalline polytypes that have a large number of applications, including temperature sensors, nanoelectromechanical systems, pressure sensors, accelerometers, and gas sensors.[26] However, not only these different crystalline polytypes of SiC are useful, attractive applications have also been reported for amorphous SiC (a-SiC), such as the detection of Salmonella,[27] Schottky barrier modulation in Schottky diodes,[28] or the manufacture of photocathodes for solar water splitting.[29]

In this sense, achieving reproducible self-formation of SiQDs within SiC matrixes could increase the plethora of applications that both systems show separately. The latter is because of the reason that the exceptional physical characteristics of SiC (wide and tunable band gaps, good thermal conductivity, adequate concentration of charge carriers, and chemical inertness) could be exploited together with the luminescent properties of SiQDs to fabricate electroluminescent structures that could operate stably at high power, high temperatures, or high voltages.

Four main research groups have studied experimental methodologies to manufacture nanoarchitectures of SiQDs inlaid in a-SiC matrixes. The group headed by Jiang and Tan studied the influence of the silane flow rate for the in situ formation of SiQDs inlaid in a-SiC films using the plasma-enhanced chemical vapor deposition (PECVD) technique.[30,31] The group of Zeng and Wen, also using the PECVD technique,

Received: March 7, 2022
Accepted: May 20, 2022
Published: June 1, 2022

© 2022 The Authors. Published by American Chemical Society

conducted studies on the influence of annealing temperature on the formation of SiQDs embedded in hydrogenated amorphous Si-rich SiC thin films.[32,33] Kole and Chaudhuri used a PECVD system to study the influence of argon dilution and subsequent heat treatments for the formation of SiQDs on a-SiC nanoarchitecture.[34,35] Finally, Kurokawa et al. used the PECVD method to study the effect of oxygen on the electrical and photoluminescent properties of superlattices based on SiQDs embedded in a-SiC thin films.[36,37]

It should be noted that, in all the aforementioned studies, the authors use the PECVD equipment. This type of system has been shown to be very reliable for obtaining SiQDs embedded in high-quality SiC thin films. However, PECVD systems have the disadvantage of gas dissociation reactions in the same area where the desired nanoarchitecture grows. Hence, much plasma-induced damage occurs in the final thin film. The plasma location also induces a more significant correlation between the deposition parameters [flow of source gases, radio frequency (RF) source power, deposition chamber pressure, substrate temperature, and deposition time]. The higher the correlation in the deposition parameters, the more difficult it is to study each parameter's influence on creating the desired nanoarchitecture and, therefore, less reproducibility.

In this regard, remote PECVD (RPECVD) systems are a convenient modification of PECVD systems.[38,39] Unlike PECVD, in the RPECVD, the gas dissociations occur in a region far from where the thin film grows. Consequently, nanostructures grown in RPECVD systems show much less plasma-induced damage. RPECVD also exhibits less correlation between deposition parameters; therefore, these systems allow the deposition of very high-quality thin films. In RPECVD systems, it is also possible to achieve excellent control of the final physical properties of the manufactured nanoarchitecture by slight adjustments of the growth parameters.[40,41] The use of RPECVD systems for depositing SiC thin films has been poorly explored.[42−45] In fact, to the best of our knowledge, to date, there is no research reporting the conformation of SiQDs embedded in SiC matrixes employing RPECVD systems. Likewise, based on the work of Matsuda[46] on the control of the formation of silicon microcrystals via plasma glow discharge, we explore in our RPECVD system the effect that different amounts of H_2 have on the luminescent properties of the deposited films, as well as in the formation of silicon nanocrystals embedded in SiC matrices.

In this work, we use an RPECVD system to grow SiC thin films on the surface of monocrystalline silicon and fused silica substrates. As a precursor gas source of silicon, we use silicon tetrachloride, a compound of complex dissociation.[47] Through complete characterization by Fourier transform infrared (FTIR) spectrophotometry, transmission and scanning electron microscopy (TEM and SEM), ultraviolet−visible (UV−vis) spectrophotometry, and spectrofluorometry (PL), we were able to determine the necessary flow of CH_4 to obtain SiC films. Likewise, we identified that a particular combination of CH_4 and H_2 mass flow allows abundant and reproducible self-formation of SiQDs within the SiC films. We observed that the PL of our SiQDs shows a normal distribution with positive skewness and well-defined intensity maxima in blue regions of the electromagnetic spectrum (439−465 nm). We consider our films to be promising for the fabrication of diverse experimental electroluminescent devices.

2. EXPERIMENTAL DETAILS

2.1. Substrate Preparation. The thin films were deposited on (200 Ω cm) single-crystalline silicon n-type wafers (100) and fused silica substrates; both substrates were purchased from UniversityWafer, Inc. Before deposition, the silicon wafers were cleaned by submerging them for 5 min in a "p-etch solution" made up of 300:15:10 of $H_2O/HNO_3/HF$, to remove impurities from the silicon surface. Additionally, quartz substrates were subject to four cycles of ultrasonic baths while immersed in (1) trichloroethylene, (2) methanol, (3) acetone, and (4) methanol, with 5 min per cycle. Both types of substrates need to be kept in the chamber for 30 min before the deposition to adequately match the sample holder temperature.

2.2. Deposition Parameters. The deposition of SiC thin films was carried out in a custom-made RPECVD system, whose detailed description can be found elsewhere.[48] The gases used in the deposition were methane (CH_4), silicon tetrachloride ($SiCl_4$), and argon (Ar). The flow rates of $SiCl_4$ and Ar were fixed at 25 and 150 sccm, respectively, while the CH_4 flow rate ranged from 12 to 20 sccm. A substrate temperature of 200 °C, a total pressure of 300 mTorr, and a RF power of 300 W were the remaining deposition parameters. In the remainder of the text, samples deposited with these parameters shall be labeled as B samples. Furthermore, another set of samples were deposited where hydrogen (H_2) was introduced to the gas mixture. In this set, the flow rates of $SiCl_4$, CH_4, and Ar were 20, 20, and 150 sccm, respectively, as the H_2 flow rate was varied from 58 to 100 sccm. The other parameters remained as follows: a substrate temperature of 480 °C, a total pressure of 400 mTorr, and an RF power of 310 W (which had to go up to 370 W for 100 sccm of H_2). These will be categorized as C samples (Table 1). After deposition, some of the samples in each set were annealed for 30 min at temperatures of 350 °C (B samples) and 600 °C (C samples).[47]

Table 1. Deposition Parameters for B and C Samples

sample	T (°C)	power (W)	pressure (mTorr)	CH_4 flow rate (sccm)	$SiCl_4$ flow rate (sccm)	Ar flow rate (sccm)	H_2 flow rate (sccm)
B1	200	300	300	20	25	150	0
B2	200	300	300	16	25	150	0
B3	200	300	300	12	25	150	0
C1	480	310	400	20	20	150	58
C2	480	310	400	20	20	150	75
C3	480	370	400	20	20	150	100

2.3. Sample Characterization. Each sample was characterized after every deposition. UV−vis transmission measurements were performed in a range of 300 to 1100 nm using a double beam PerkinElmer Lambda 35 UV−vis spectrophotometer. Chemical bonds were identified using a FTIR spectrophotometer, Nicolet 210, in the region of 4000 to 350 cm^{-1}. PL measurements were obtained in a dark room at room temperature, using a Kimmon helium−cadmium laser beam operating with a wavelength of 325 nm and a power of 25 mW. The PL spectra were recorded with a Fluoromax-Spex spectrofluorometer. The laser had an incidence angle of 45° to the thin film, while the angle of detection of the emitted light was normal to the film surface. The thickness of SiC thin films

was measured using a scanning electron microscope JSM-7800F. SEM micrographs were captured at an accelerating voltage of 5 keV to limit the nonconductive SiC coating charging effects and a magnification of ×80,000. High-resolution transmission electron microscopy (HRTEM) analysis was performed using a JEOL JEM-2010F FasTEM microscope, which was operated at an acceleration voltage of 200 kV.

3. RESULTS AND DISCUSSION

The thickness and deposition rate values for B samples are shown in Table 2, in which we can appreciate that the deposition rate increases with the flow rate of methane. Meanwhile, the FTIR spectra for samples B1, B2, and B3 before and after annealing are shown in Figure 1. One can identify that all samples have three prominent peaks, with the first one being centered at around 3400 cm^{-1}, attributed to the vibration of N−H stretching bonds.[49] The peak centered at around 1035 cm^{-1} corresponds to an sp^3 CH_2 bonded to Si, but it can also be attributed to oxygen vibrational modes such as Si−O−Si and Si−O−C stretching.[50] Then, the peaks at 846 cm^{-1} for the as-grown sample and at 795 cm^{-1} for the cured sample could correspond to Si−C stretching bonds.[51] As the methane flux increases, the growth of this type of bond in the as-grown B-group films may be related to the increase in the deposition rate observed previously. Additionally, the as-grown sample B3 presents a peak at 2326 cm^{-1} consistent with the vibration of the Si−H bond,[52] which, together with the N−H bond, is predominant at low deposition rates. As we could have expected, when the CH_4 flow rate diminished, the C−H peak decreases significantly. The samples that were annealed at 350 °C had an increment in the peak centered at 1035 cm^{-1} with respect to the other two peaks (at around 3430 and 795 cm^{-1}), possibly due to the incorporation of oxygen when the samples were annealed.

Table 2. Thicknesses and Deposition Rates of Samples as the Methane Flow Rate Is Varied from 12 to 20 sccm

sample	thickness (nm)	deposition rate (nm/min)	CH_4 flow rate (sccm)
B1	336.3 ± 7.7	22.4 ± 0.5	20
B2	238.3 ± 4.7	15.8 ± 0.3	16
B3	63.8 ± 4.2	4.2 ± 0.3	12

Figure 2 shows the PL spectra of samples B1, B2, and B3 before (black line) and after annealing at 350 °C (red line). All samples present an emission band from 390 to 450 nm. Likewise, it is possible to identify in the as-grown samples that as the CH_4 flux increases the maximum emission peak moves toward the green region (∼500 nm), which could be attributed to the increase in Si−C and/or N−H bonds with respect to the increase in methane flux (attributable to the Si−C or N−H bonds present in the film). It is also interesting to note that this green shift peak in the samples with the highest CH_4 flux increases after annealing, which could be related to the increase in Si−CH_2 and Si−C bonds observed in the infrared spectra, as well as to the probable presence of oxygen in the sample, mentioned above when discussing Figure 1.

Various studies have shown that H_2 gas promotes crystallization in silicon-based films; this is achieved, thanks to the hydrogen terminations on the surface of the substrate, which causes the silicon atoms to migrate to the surface. This process places the silicon atoms in favorable places for crystallization.[46,53] With this knowledge, we added hydrogen to our gas mixture with the motivation to explore the degree of crystallization we would achieve in our final structures with different amounts of H_2. Table 3 shows the thickness of the C samples, where we can appreciate an increase in the deposition rate as the H_2 flow augments.

Figure 3 shows the FTIR absorbance spectra of samples C1, C2, and C3 before and after annealing at 600 °C for 30 min. The signal-to-noise ratio is low due to the thickness of the sample. Nevertheless, the principal peaks can still be identified. Before annealing, all the samples had the most prominent peaks from the Si−C bond vibration (803 cm^{-1}), indicating that most of the bonds were of Si−C. The latter could also be corroborated qualitatively, as the film did not get scratches from the tweezers, proving the hardness of the film (which is a quality of SiC films). Additionally, it is worth noticing that the N−H peaks were not present in this set of samples, in contrast with group B samples. The latter may be due to the passivation of the surface achieved with H_2, unlike the samples of group B,

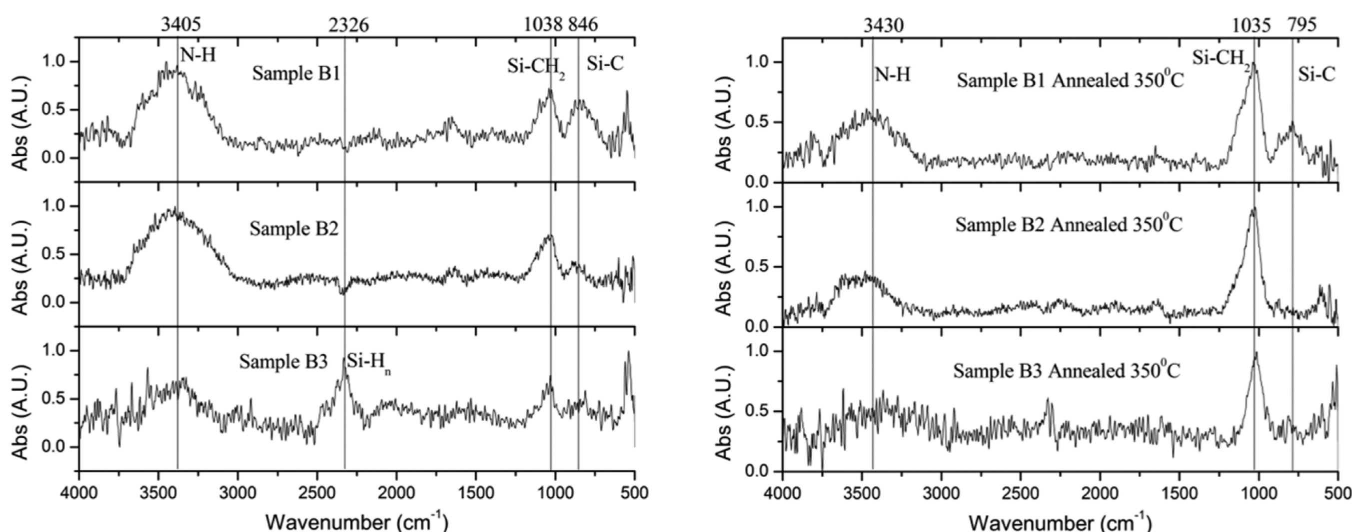

Figure 1. . FTIR absorbance spectrum of samples B1, B2, and B3 before (left) and after (right) annealing at 350 °C for 30 min. The vertical lines correspond to the wavenumber that is centered at each peak.

https://doi.org/10.1021/acsomega.2c01384
ACS Omega 2022, 7, 19640−19647

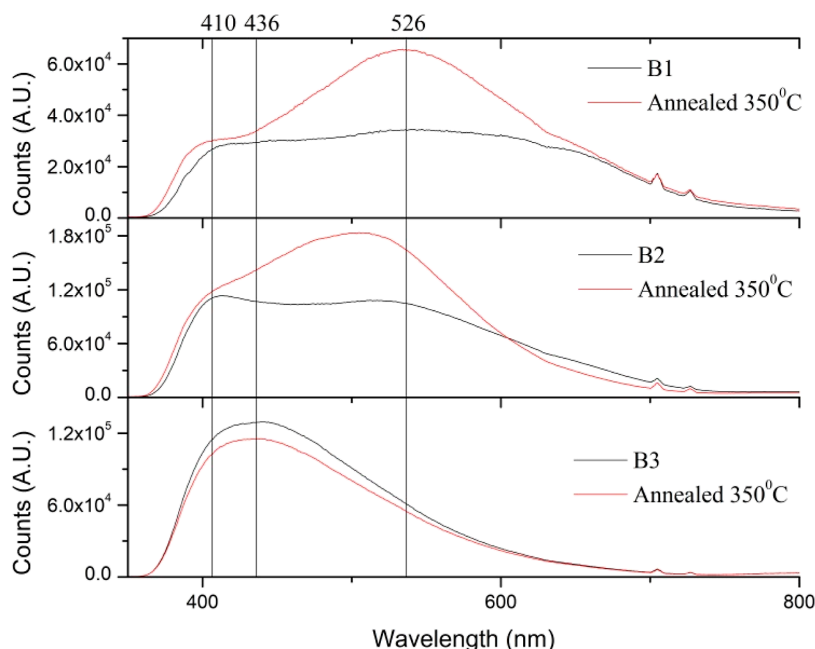

Figure 2. PL spectra of samples B1, B2, and B3 before (black line) and after annealing (red line) at 350 °C for 30 min. The vertical lines indicate the wavelengths at the center of the peaks.

Table 3. Thicknesses and Deposition Rates of the Samples When the Hydrogen Flow Rate Is Varied from 58 to 100 sccm

sample	thickness (nm)	deposition rate (nm/min)	H_2 flow rate (sccm)
C1	34.7 ± 5.2	2.31 ± 0.34	58
C2	123.2 ± 3.6	8.2 ± 0.24	75
C3	250.4 ± 4.2	10.0 ± 0.16	100

whose terminations can bind to ambient nitrogen and oxygen.[54,55] With thermal annealing, Si−CH_2 (1024 cm^{-1}) bonds grew compared to the other peaks.

The SiC thin film's band gaps as a function of methane and hydrogen were calculated from the data collected from the UV−vis transmission spectra of the annealed films using Tauc's method and are shown in Figure 4. There is a clear tendency in which the band gap increases as both the methane and hydrogen flow increases. As the methane flow increases, so does the film's carbon content, meaning that the band gap tends to be that of a carbon thin film, which is higher than the band gap of amorphous silicon thin films. Thus, explaining the increase in the band gap as the carbon content augments.[56] On the other hand, the increase in the band gap as the hydrogen flow increases can be attributed to replacing the Si−Si bonds (as they are the weaker ones) with the Si−H bonds (which can be seen in Figure 3). As the Si−H bonds have a more stable bond, a higher energy will be required to remove an electron, thus creating a higher band gap.[57] Other publications attribute this increase in the band gap to the reduction of the relative concentration of sp^2-bonded carbon.[58] It is also worth noting

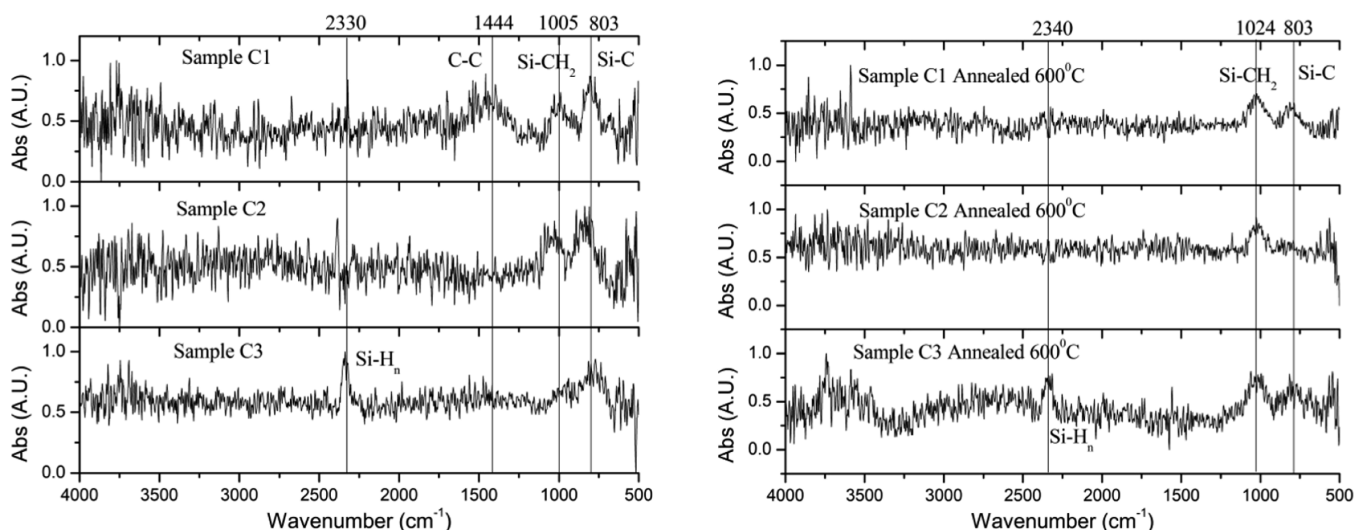

Figure 3. FTIR absorbance spectrum of samples C1, C2, and C3 before and after annealing at 600 °C for 30 min. The vertical lines show the wavenumber at the center of each peak and its corresponding bond tag.

https://doi.org/10.1021/acsomega.2c01384
ACS Omega 2022, 7, 19640−19647

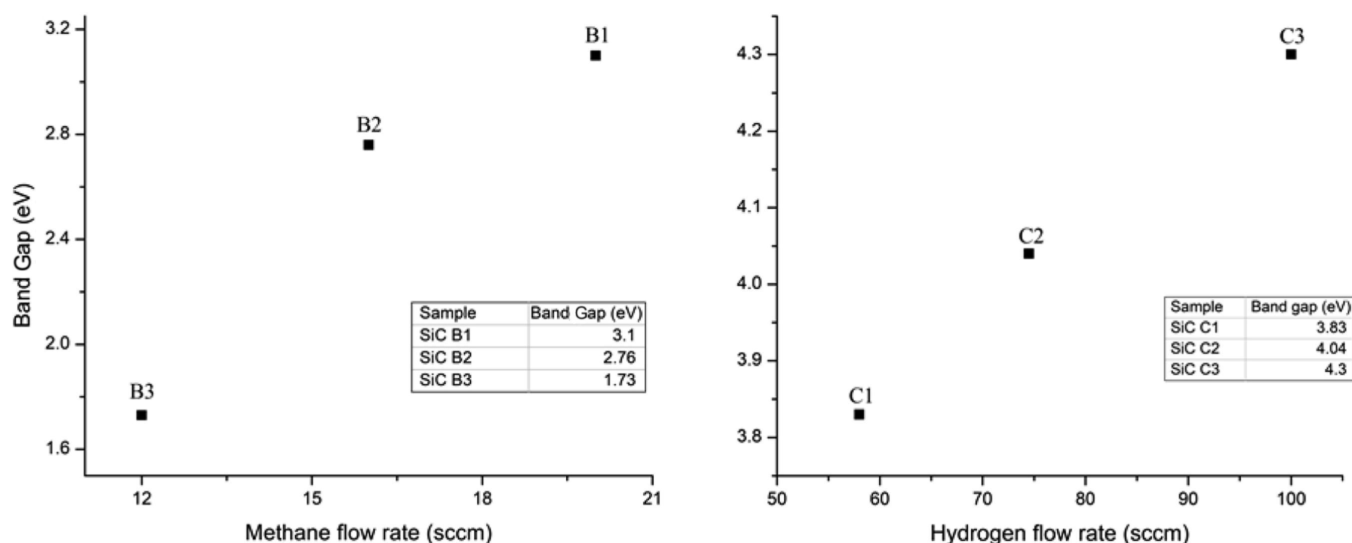

Figure 4. Band gaps of group B samples (left) and group C samples (right), in function of the methane and hydrogen flow rate, respectively.

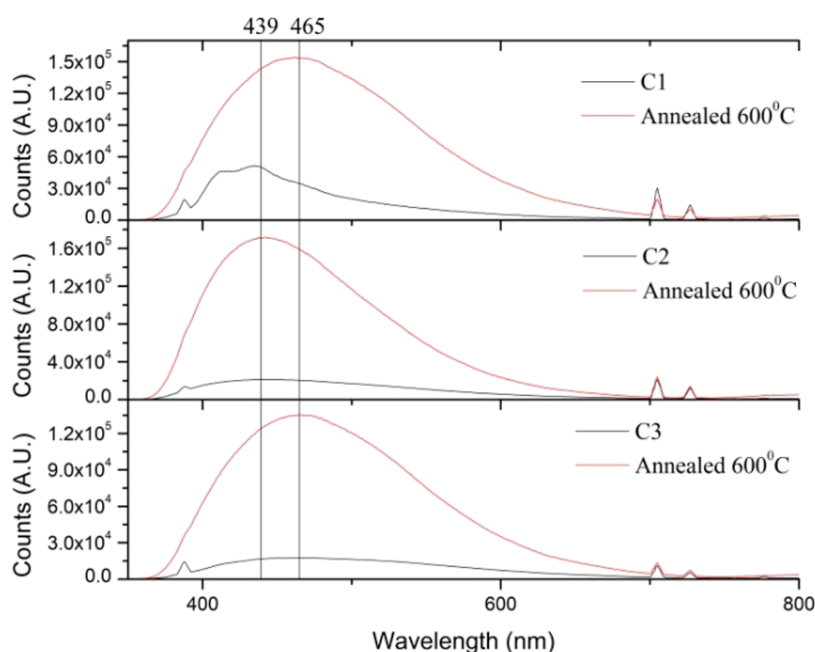

Figure 5. PL spectra of samples C1, C2, and C3 before (black line) and after annealing (red line) at 600 °C for 30 min. The vertical lines show that the center of the peaks are at 439 and 465 nm for as-grown and annealed samples, respectively.

that the band gap values were considerably larger (from 3.83 to 4.3 eV) with these conditions as opposed to the previous ones (1.73 to 3.1 eV).

Furthermore, PL spectra for samples C1, C2, and C3 are shown in Figure 5. All samples exhibit a peak in the blue region, unlike the group B samples, where there was another peak present (Figure 2). This could be related to the passivation achieved in these C samples, unlike group B samples. Absence of N−H bonds or increase in the peaks located at around 1035 cm^{-1} was observed, also related to Si−O−Si bonds in IR spectra. However, it can also be attributed to the lack of N−H bonds in group C samples. Another difference that can be highlighted is that the annealing of the samples implied an increase of nearly 1 order of magnitude in the PL (with PL perceptible to the naked eye), which could be related to the crystallization of the films at this high temperature (600 °C) by reducing grain effects and, therefore, non-radiative recombination. However, further work is required to determine the origin of this increase in PL after annealing. The change in hydrogen flow did not affect the PL spectra as both the annealed and as-deposited samples exhibited the same behavior.

Finally, Figure 6 shows TEM micrographs of the annealed samples C1, C2, and C3 to study the microstructure of the SiC thin films. As previously mentioned, hydrogen assists the crystallization of the film. However, not only hydrogen but also a heat treatment is necessary for the formation of nanoclusters, which can be appreciated as the darker spots in the micrographs. As greater magnification is applied, the orientation of the planes in the lattice can be visible (Figure 6c). An electron diffraction pattern confirms the formation of a crystalline phase, as shown in Figure 6d. H_2 flow influenced the

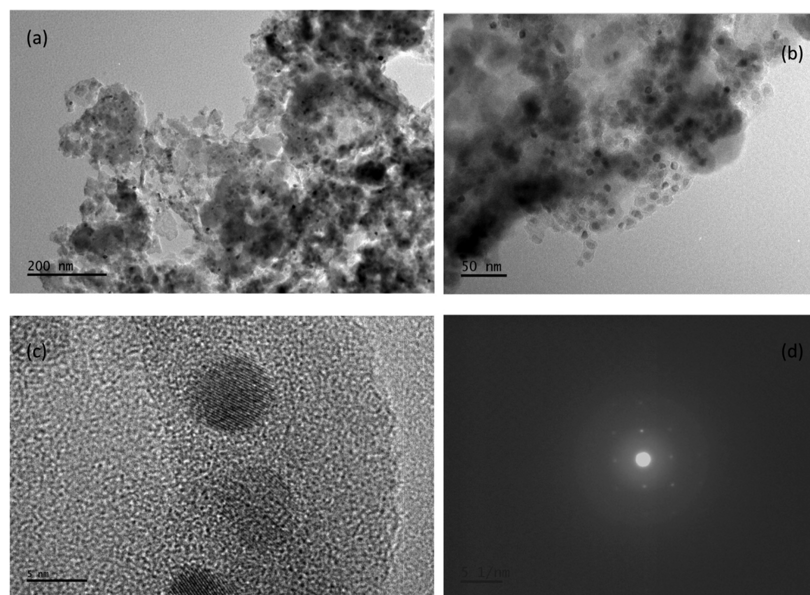

Figure 6. TEM micrographs for samples (a) C1, (b) C2, and (c) C3 showing the presence of nanoclusters, where the orientation of the planes can also be appreciated. (d) Selected area diffraction pattern of a SiQD.

size of the nanocluster, as can be seen in Table 4 because the average particle size decreases as the hydrogen flow increases.

Table 4. Average Particle Size and Band Gap as a Function of Hydrogen Flow

sample	particle average size (nm)	band gap (eV)	hydrogen flow rate (sccm)
C1	10.54 ± 0.78	3.83	58
C2	9.76 ± 0.56	4.04	75
C3	7.97 ± 0.64	4.3	100

Moreover, the band gap also increases as the particle size reduces. The latter is congruent to the particle in a box model where the energy levels permitted have an inversely proportional dependency on the size of the box, where, in this case, the box is the nanocluster.[59]

4. CONCLUSIONS

We achieved a reproducible growth of a-SiC films using a custom-made RPECVD system. We employed a gas mixture of methane, argon, and silicon tetrachloride. We identified that by increasing the methane gas flux, a PL shift is obtained toward the green zone of the electromagnetic spectrum (526 nm). Likewise, the annealing of these films at a relatively low temperature (350 °C) caused the increase in their PL-integrated intensity, probably due to the oxygen incorporation after the thermal treatment in a conventional furnace, as observed in the IR spectra.

Once the SiC films were obtained, we proceeded to add different amounts of H_2 to the original gas mixture to explore the effect this gas has on the physical properties of the films (group C samples). All group C samples exhibit a PL peak in the blue region, which can be attributed to the passivation achieved in C samples, due to the presence of H_2. Likewise, we have observed that annealing at 600 °C in the films grown with H_2 promotes the formation of silicon nanocrystals embedded in the SiC film, as observed in TEM images. These SiQDs dramatically increase the integrated intensity of PL, which may be caused by the crystallization achieved after heat treatment of the films. The maximum spectral intensity of these films is located in the blue region of the electromagnetic spectrum (between 439 and 465 nm) and is perceptible to the naked eye.

■ ASSOCIATED CONTENT

Supporting Information

The Supporting Information is available free of charge at https://pubs.acs.org/doi/10.1021/acsomega.2c01384.

Cross-sectional SEM micrographs, transmittance spectra of B and C group samples, Tauc method, and Tauc plots for B and C group samples (PDF)

■ AUTHOR INFORMATION

Corresponding Author

Arturo Rodríguez-Gómez − *Instituto de Física, Universidad Nacional Autónoma de México, Ciudad de México 04510, México;* orcid.org/0000-0003-1331-8598; Email: arodriguez@fisica.unam.mx

Authors

Rodrigo León-Guillén − *Instituto de Física, Universidad Nacional Autónoma de México, Ciudad de México 04510, México*

Ana Luz Muñoz-Rosas − *Instituto de Física, Universidad Nacional Autónoma de México, Ciudad de México 04510, México*

Jesús A. Arenas-Alatorre − *Instituto de Física, Universidad Nacional Autónoma de México, Ciudad de México 04510, México*

Juan Carlos Alonso-Huitrón − *Instituto de Investigaciones en Materiales, Universidad Nacional Autónoma de México, Ciudad de México 04510, México*

Ana Laura Pérez-Martínez − *Facultad de Ingeniería, División de Ciencias Básicas, Universidad Nacional Autónoma de México, Ciudad de México 04510, México*

Complete contact information is available at:

https://doi.org/10.1021/acsomega.2c01384
ACS Omega 2022, 7, 19640−19647

https://pubs.acs.org/10.1021/acsomega.2c01384

Notes

The authors declare no competing financial interest.
The data that support the findings of this study are available within the article.

■ ACKNOWLEDGMENTS

The first author is grateful to CONACYT for granting Doctoral Fellowship CVU number: 896712. The authors express their gratitude to Juan Gabriel Morales Morales and Diego Quiterio for sample preparation and for observation by electron microscopy. The authors also would like to acknowledge Roberto Hernández Reyes and Samuel Tehuacanero Cuapa for their technical assistance in TEM and SEM analyses. This research work was financially supported by projects: (a) PAPIIT-UNAM, project number: IN109020 and (b) Investigación Científica Básica SEP—CONACYT project number: 283492. All the authors acknowledge and appreciate the invaluable labor and courage of all those who, during the tragic COVID-19 pandemic, exposed their lives to keep doing first necessity activities for society's good. The corresponding author declares his faith and gratitude to the Almighty.

■ REFERENCES

(1) Lacerda, V. R.; Acevedo, A. F. G.; Marques, I. C. d. S.; Dellabiglia, W. J.; Ferraz, A. K. L.; Basílio, L. S. P.; Broetto, F. Silicon as a Mitigator of Water Deficit Stress in Radish Crop. *Sci. Hortic. (Amsterdam, Neth.)* **2022**, *291*, 110600.
(2) Mock, J.; Groß, E.; Kloberg, M. J.; Rieger, B.; Becherer, M. Surface Engineering of Silicon Quantum Dots: Does the Ligand Length Impact the Optoelectronic Properties of Light-Emitting Diodes? *Adv. Photonics Res.* **2021**, *2*, 2100083.
(3) Kayanuma, Y. Quantum-Size Effects of Interacting Electrons and Holes in Semiconductor Microcrystals with Spherical Shape. *Phys. Rev. B: Condens. Matter Mater. Phys.* **1988**, *38*, 9797−9805.
(4) Serrano-Núñez, M. A.; Rodríguez-Gómez, A.; Escobar-Alarcón, L.; Alonso-Huitrón, J. C. Combined Study of the Effect of Deposition Temperature and Post-Deposition Annealing on the Photoluminescence of Silicon Quantum Dots Embedded in Chlorinated Silicon Nitride Thin Films. *RSC Adv.* **2016**, *6*, 77440−77451.
(5) Kim, T.-Y.; Park, N.-M.; Kim, K.-H.; Sung, G. Y.; Ok, Y.-W.; Seong, T.-Y.; Choi, C.-J. Quantum Confinement Effect of Silicon Nanocrystals in Situ Grown in Silicon Nitride Films. *Appl. Phys. Lett.* **2004**, *85*, 5355.
(6) Kim, T.-W.; Cho, C.-H.; Kim, B.-H.; Park, S.-J. Quantum Confinement Effect in Crystalline Silicon Quantum Dots in Silicon Nitride Grown Using SiH4 and NH3. *Appl. Phys. Lett.* **2006**, *88*, 123102.
(7) Torchynska, T.; Khomenkova, L.; Slaoui, A. Modification of Light Emission in Si-Rich Silicon Nitride Films Versus Stoichiometry and Excitation Light Energy. *J. Electron. Mater.* **2018**, *47*, 3927−3933.
(8) Hafsi, N.; Bouridah, H.; Boutaoui, N. Effect of the Reflection by the Silicon Aggregates on the Photoluminescence from Silicon Nitride Film Embedded Silicon Nanocrystals. *Mater. Sci. Semicond. Process.* **2017**, *68*, 334−338.
(9) Zhigunov, D. M.; Kamenskikh, I. A.; Lebedev, A. M.; Chumakov, R. G.; Logachev, Y. A.; Yakunin, S. N.; Kashkarov, P. K. X-Ray Reflectivity and Photoelectron Spectroscopy of Superlattices with Silicon Nanocrystals. *JETP Lett.* **2017**, *106*, 517−521.
(10) Muñoz-Rosas, A. L.; Rodríguez-Gómez, A.; Arenas-Alatorre, J. A.; Alonso-Huitrón, J. C. Photoluminescence Enhancement from Silicon Quantum Dots Located in the Vicinity of a Monolayer of Gold Nanoparticles. *RSC Adv.* **2015**, *5*, 92923−92931.
(11) Rodríguez-Gómez, A.; Moreno-Rios, M.; García-García, R.; Pérez-Martínez, A. L.; Reyes-Gasga, J. Role of the Substrate on the Growth of Silicon Quantum Dots Embedded in Silicon Nitride Thin Films. *Mater. Chem. Phys.* **2018**, *208*, 61−67.
(12) Watanabe, J.; Yamada, H.; Sun, H.-T.; Moronaga, T.; Ishii, Y.; Shirahata, N. Silicon Quantum Dots for Light-Emitting Diodes Extending to the NIR-II Window. *ACS Appl. Nano Mater.* **2021**, *4*, 11651.
(13) Milliken, S.; Cui, K.; Klein, B. A.; Cheong, I. T.; Yu, H.; Michaelis, V. K.; Veinot, J. G. C. Tailoring B-Doped Silicon Nanocrystal Surface Chemistry via Phosphorous Pentachloride − Mediated Surface Alkoxylation. *Nanoscale* **2021**, *13*, 18281−18292.
(14) Chen, J.; Yu, Y.; Zhu, B.; Han, J.; Liu, C.; Liu, C.; Miao, L.; Fakudze, S. Synthesis of Biocompatible and Highly Fluorescent N-Doped Silicon Quantum Dots from Wheat Straw and Ionic Liquids for Heavy Metal Detection and Cell Imaging. *Sci. Total Environ.* **2021**, *765*, 142754.
(15) Lin, Z.; Guo, Y.; Lin, Z.; Song, J.; Zhang, Y.; Song, C.; Huang, R. Enhanced Red Light Emission from Dense Si Quantum Dot-Based Silicon Oxynitride Light-Emitting Diodes with Reduced Efficiency Droop. *J. Lumin.* **2020**, *222*, 117138.
(16) Morozova, S.; Alikina, M.; Vinogradov, A.; Pagliaro, M. Silicon Quantum Dots: Synthesis, Encapsulation, and Application in Light-Emitting Diodes. *Front. Chem.* **2020**, *8*, 1−8.
(17) Yamada, H.; Saitoh, N.; Ghosh, B.; Masuda, Y.; Yoshizawa, N.; Shirahata, N. Improved Brightness and Color Tunability of Solution-Processed Silicon Quantum Dot Light-Emitting Diodes. *J. Phys. Chem. C* **2020**, *124*, 23333−23342.
(18) Terada, S.; Xin, Y.; Saitow, K.-i. Cost-Effective Synthesis of Silicon Quantum Dots. *Chem. Mater.* **2020**, *32*, 8382−8392.
(19) Liu, Z.; Hou, J.; Wang, X.; Hou, C.; Ji, Z.; He, Q.; Huo, D. A Novel Fluorescence Probe for Rapid and Sensitive Detection of Tetracyclines Residues Based on Silicon Quantum Dots. *Spectrochim. Acta, Part A* **2020**, *240*, 118463.
(20) Pradhan, S.; Das, S. R.; Nanda, B. K.; Jena, P. C.; Dhupal, D. Experimental Investigation on Machining of Hardstone Quartz with Modified AJM Using Hot Silicon Carbide Abrasives. *J. Braz. Soc. Mech. Sci. Eng.* **2020**, *42*, 1−22.
(21) Saravanan, C.; Dinesh, S.; Sakthivel, P.; Vijayan, V.; Kumar, B. S. Assessment of Mechanical Properties of Silicon Carbide and Graphene Reinforced Aluminium Composite. *Mater. Today: Proc.* **2020**, *21*, 744−747.
(22) Lukin, D. M.; Guidry, M. A.; Vučković, J. Silicon Carbide: From Abrasives to Quantum Photonics. *Opt. Photonics News* **2021**, *32*, 34.
(23) Lukin, D. M.; Guidry, M. A.; Vučković, J. Integrated Quantum Photonics with Silicon Carbide: Challenges and Prospects. *PRX Quantum* **2020**, *1*, 020102.
(24) Tarasenko, S. A.; Poshakinskiy, A. V.; Simin, D.; Soltamov, V. A.; Mokhov, E. N.; Baranov, P. G.; Dyakonov, V.; Astakhov, G. V. Spin and Optical Properties of Silicon Vacancies in Silicon Carbide—A Review. *Phys. Status Solidi* **2018**, *255*, 1700258.
(25) Castelletto, S.; Boretti, A. Silicon Carbide Color Centers for Quantum Applications. *J. Phys.: Photonics* **2020**, *2*, 022001.
(26) Xu, M.; Girish, Y. R.; Rakesh, K. P.; Wu, P.; Manukumar, H. M.; Byrappa, S. M.; Udayabhanu; Byrappa, K. Recent Advances and Challenges in Silicon Carbide (SiC) Ceramic Nanoarchitectures and Their Applications. *Mater. Today Commun.* **2021**, *28*, 102533.
(27) Gómez-Montaño, F. J.; Orduña-Díaz, A.; Avelino-Flores, M. d. C. G.; Avelino-Flores, F.; Reyes-Betanzo, C.; Rojas-López, M. Determination of Salmonella Typhimurium by Fourier Transform Infrared (FTIR) Spectroscopy Using a Hydrogenated Amorphous Silicon Carbide (a-SiC:H) Thin Film. *Anal. Lett.* **2021**, *54*, 2655−2665.
(28) Triendl, F.; Pfusterschmied, G.; Berger, C.; Schwarz, S.; Artner, W.; Schmid, U. Ti/4H-SiC Schottky Barrier Modulation by Ultrathin a-SiC:H Interface Layer. *Thin Solid Films* **2021**, *721*, 138539.
(29) Mejia, M. D. C.; Sánchez, L. F.; Kurniawan, M.; Eggert, L.; Tejada, A.; Camargo, M.; Grieseler, R.; Rumiche, F.; Díaz, I.; Bund, A.; Guerra, J. A. Analysis of the Physical and Photoelectrochemical

Properties of C-Si(p)/a-SiC:H(p) Photocathodes for Solar Water Splitting. *J. Phys. D: Appl. Phys.* **2021**, *54*, 269601.

(30) Li, M.; Jiang, L.; Peng, Y.; Wang, T.; Xiao, T.; Xiang, P.; Tan, X. The Evolution of PL Properties of Hydrogenated Si-Rich Silicon Carbide/Amorphous Carbon Nano-Multilayer Films Grown by PECVD. *Optik* **2019**, *176*, 401−409.

(31) Jiang, L.; Tan, X.; Xiao, T.; Xiang, P.; Li, J. In Situ-Grown Silicon Quantum Dots in SiCx:H/a-C:H Hetero-Multilayer Films Prepared by Plasma Enhanced Chemical Vapor Deposition Method. *J. Alloys Compd.* **2017**, *718*, 116−121.

(32) Wen, G.; Zeng, X.; Li, X. The Influence of Annealing Temperature on the Synthesis of Silicon Quantum Dots Embedded in Hydrogenated Amorphous Si-Rich Silicon Carbide Matrix. *J. Non-Cryst. Solids* **2016**, *441*, 10−15.

(33) Wen, G.; Zeng, X.; Wen, X.; Liao, W. Photoluminescence Properties and Crystallization of Silicon Quantum Dots in Hydrogenated Amorphous Si-Rich Silicon Carbide Films. *J. Appl. Phys.* **2014**, *115*, 164303.

(34) Kole, A.; Chaudhuri, P. Growth of Silicon Quantum Dots by Oxidation of the Silicon Nanocrystals Embedded within Silicon Carbide Matrix. *AIP Adv.* **2014**, *4*, 107106.

(35) Kole, A.; Chaudhuri, P. Nanocrystalline Silicon and Silicon Quantum Dots Formation within Amorphous Silicon Carbide by Plasma Enhanced Chemical Vapour Deposition Method Controlling the Argon Dilution of the Process Gases. *Thin Solid Films* **2012**, *522*, 45−49.

(36) Kurokawa, Y.; Yamada, S.; Miyajima, S.; Yamada, A.; Konagai, M. Effects of Oxygen Addition on Electrical Properties of Silicon Quantum Dots/Amorphous Silicon Carbide Superlattice. *Curr. Appl. Phys.* **2010**, *10*, S435−S438.

(37) Kurokawa, Y.; Tomita, S.; Miyajima, S.; Yamada, A.; Konagai, M. Photoluminescence from Silicon Quantum Dots in Si Quantum Dots/Amorphous SiC Superlattice. *Jpn. J. Appl. Phys.* **2007**, *46*, L833−L835.

(38) Rodríguez-Gómez, A.; Escobar-Alarcón, L.; Serna, R.; Cabello, F.; Haro-Poniatowski, E.; García-Valenzuela, A.; Alonso, J. C. Modeling of the Refractive Index and Composition of Luminescent Nanometric Chlorinated-Silicon Nitride Films with Embedded Si-Quantum Dots. *J. Appl. Phys.* **2016**, *120*, 145305.

(39) Rodríguez, A.; Arenas, J.; Pérez-Martínez, A. L.; Alonso, J. C. Role of Ammonia in Depositing Silicon Nanoparticles by Remote Plasma Enhanced Chemical Vapor Deposition. *Mater. Lett.* **2014**, *125*, 44−47.

(40) Claflin, B.; Grzybowski, G. J.; Ware, M. E.; Zollner, S.; Kiefer, A. M. Process for Growth of Group-IV Alloys Containing Tin by Remote Plasma Enhanced Chemical Vapor Deposition. *Front. Mater.* **2020**, *7*, 1−6.

(41) Borah, R.; Das, S.; Sharma, A.; Dutta, A. A Review on Various Techniques Implemented for the Synthesis of SiliconCarbo-Nitride (SiCN) Coatings. *AIP Conference Proceedings*; AIP Publishing LLC, 2020; Vol. *2273*, p 040007.

(42) Kosinova, M. L.; Fainer, N. I.; Rumyantsev, Y. M.; Terauchi, M.; Shibata, K.; Satoh, F.; Tanaka, M.; Kuznetsov, F. A. Structure and Composition Investigation of RPECVD SiCN and LPCVD BCN Films. *J. phys., IV* **2001**, *11*, 987−994.

(43) Fainer, N. I.; Kosinova, M. L.; Rumyantsev, Y. M.; Kuznetsov, F. A. RPECVD Thin Silicon Carbonitride Films Using Hexamethyldisilazane. *J. phys., IV* **1999**, *09*, 769−775.

(44) Gölz, A.; Gro*β*, S.; Janssen, R.; Stein von Kamienski, E.; Kurz, H. Fabrication of High-Quality Oxides on SiC by Remote PECVD. *Diamond Relat. Mater.* **1997**, *6*, 1420−1423.

(45) Gölz, A.; Groß, S.; Janssen, R.; von Kamienski, E. S.; Kurz, H. Electrical Properties of Oxides on Silicon Carbide Grown by Remote Plasma Chemical Vapor Deposition Annealed in Different Gas Ambients. *Mater. Sci. Eng. B* **1997**, *46*, 363−365.

(46) Matsuda, A.; Yoshida, T.; Yamasaki, S.; Tanaka, K. Structural Study on Amorphous-Microcrystalline Mixed-Phase Si:H Films. *Jpn. J. Appl. Phys.* **1981**, *20*, L439−L442.

(47) Yonekubo, S.; Tanaka, H.; Kamimura, K.; Onuma, Y. Preparation of SiC Thin Films by Plasma-Enhanced Chemical Vapor Deposition Using Silicon Tetrachloride. *IEEJ Trans. Fundam.* **1995**, *115*, 770−774.

(48) Rodriguez-Gómez, A.; García-Valenzuela, A.; Haro-Poniatowski, E.; Alonso-Huitrón, J. C. Effect of Thickness on the Photoluminescence of Silicon Quantum Dots Embedded in Silicon Nitride Films. *J. Appl. Phys.* **2013**, *113*, 233102.

(49) Pretsch, E.; Bühlmann, P.; Badertscher, M. *Structure Determination of Organic Compounds*; Springer Berlin Heidelberg: Berlin, Heidelberg, 2020.

(50) Kim, D. S.; Lee, Y. H. Annealing Effects on A-SiC:H and a-SiC:H(F) Thin Films Deposited by PECVD at Room Temperature. *Thin Solid Films* **1995**, *261*, 192−201.

(51) Basa, D. K.; Smith, F. W. Annealing and Crystallization Processes in a Hydrogenated Amorphous Si·C Alloy Film. *Thin Solid Films* **1990**, *192*, 121−133.

(52) Brodsky, M. H.; Cardona, M.; Cuomo, J. J. Infrared and Raman Spectra of the Silicon-Hydrogen Bonds in Amorphous Silicon Prepared by Glow Discharge and Sputtering. *Phys. Rev. B: Solid State* **1977**, *16*, 3556−3571.

(53) Matsuda, A. Formation Kinetics and Control of Microcrystallite in Mc-Si:H from Glow Discharge Plasma. *J. Non-Cryst. Solids* **1983**, *59-60*, 767−774.

(54) Seyller, T. Passivation of Hexagonal SiC Surfaces by Hydrogen Termination. *J. Phys.: Condens. Matter* **2004**, *16*, S1755−S1782.

(55) Santana, G.; Monroy, B. M.; Ortiz, A.; Huerta, L.; Alonso, J. C.; Fandiño, J.; Aguilar-Hernández, J.; Hoyos, E.; Cruz-Gandarilla, F.; Contreras-Puentes, G. Influence of the Surrounding Host in Obtaining Tunable and Strong Visible Photoluminescence from Silicon Nanoparticles. *Appl. Phys. Lett.* **2006**, *88*, 041916.

(56) Hsu, C.-H.; Zhang, X.-Y.; Zhao, M. J.; Lin, H.-J.; Zhu, W.-Z.; Lien, S.-Y. Silicon Heterojunction Solar Cells with P-Type Silicon Carbon Window Layer. *Crystals* **2019**, *9*, 402.

(57) Steffens, J.; Rinder, J.; Hahn, G.; Terheiden, B. Correlation between the Optical Bandgap and the Monohydride Bond Density of Hydrogenated Amorphous Silicon. *J. Non-Cryst. Solids: X* **2020**, *5*, 100044.

(58) Park, M.; Teng, C. W.; Sakhrani, V.; McLaurin, M. B.; Kolbas, R. M.; Sanwald, R. C.; Nemanich, R. J.; Hren, J. J.; Cuomo, J. J. Optical Characterization of Wide Band Gap Amorphous Semiconductors (a-Si:C:H): Effect of Hydrogen Dilution. *J. Appl. Phys.* **2001**, *89*, 1130−1137.

(59) Singh, M.; Goyal, M.; Devlal, K. Size and Shape Effects on the Band Gap of Semiconductor Compound Nanomaterials. *J. Taibah Univ. Sci.* **2018**, *12*, 470−475.

https://doi.org/10.1021/acsomega.2c01384
ACS Omega 2022, 7, 19640−19647